

Response Capacity Allocation of Air Conditioners for Peak-Valley Regulation Considering Interaction with Surrounding Microclimate

Zhenwei Zhang, *Graduate Student Member, IEEE*, Hongxun Hui, *Member, IEEE*,
and Yonghua Song, *Fellow, IEEE*

Abstract—The proliferation of air conditioners (ACs) has established them as vital demand response resources in urban power systems. The energy consumption of ACs is directly determined by the surrounding microclimate, while the corresponding waste heat raises the ambient temperature. In this paper, we study the capacity allocation of ACs for demand response considering interaction with surrounding microclimate. First, a unified thermal model integrated with ACs and urban microclimate is established to analyze the micro-scale heat flux transfer. This thermal model can quantify the interactions between extra energy demand of ACs and rising temperature of building blocks. Second, we formulate a two-stage optimal response capacity allocation model of ACs for providing peak-valley regulation services. In the first stage, load aggregators (LAGs) engage in a cooperative game to maximize response benefits considering response revenues as well as indoor and outdoor temperature deviation penalties. In the second stage, the LAGs implement state-of-charge equalization to allocate the first-stage capacity, enforcing consistent comfort levels for individual buildings. Additionally, we design a parameter equivalence and differential linearization algorithm to solve model efficiently. Finally, we validate the proposed method on all 4,739 individual buildings in the Macau Peninsula. Numerical results show that the proposed strategy can effectively increase the response benefits and satisfy individual comfort requirements.

Index Terms—Air conditioner, demand response, capacity allocation, urban microclimate.

I. INTRODUCTION

THE integration of high penetration intermittent renewable energy sources necessitates additional reserve resources to mitigate peak-to-valley fluctuations [1]. Compared to traditional thermal and gas-fired units, demand-side resources, such as air conditioners (ACs), offer significant regulation potential with lower carbon emission and higher response capability [2]. With advancements in Internet of Things (IoT) technologies, ACs can effectively provide operation reserve by utilizing the building's thermal inertia [3]. Until 2023, roughly 2 billion ACs are in operation around the world [4]. Specifically, in power system, ACs contribute to 20% of the peak cooling load in China and account for over 70% of residential electrical demand during extremely hot days [5]. The rapid proliferation

This work was funded in part by the National Natural Science Foundation of China (Grant No. 52407075), in part by the Science and Technology Development Fund, Macau SAR (File no. 001/2024/SKL, and no. 0117/2022/A3), and in part by the Chair Professor Research Grant of University of Macau (File no. CPG2024-00015-IOTSC). (Corresponding author: *Hongxun Hui*.)

Z. Zhang, H. Hui and Y. Song are with the State Key Laboratory of Internet of Things for Smart City and Department of Electrical and Computer Engineering, University of Macau, Macao, China. (email: hongxun-hui@um.edu.mo)

of ACs has garnered considerable attention on its involvement in demand response, i.e., load shifting [6], [7], frequency regulation [8], [9] and voltage control [10], [11].

Several studies have examined ACs in various demand response scenarios, categorizing them into two main models [12]. The Equivalent Thermal Parameter (ETP) model is particularly notable for its extensive application in capturing the dynamic thermal characteristics of buildings [13]. In [14], a multi-time scale coordinated scheduling strategy using ETP is proposed to address microgrid tie flow. To accurately assess thermal comfort for residents, the Monte Carlo simulation method is applied within the ETP to mimic real-life scenarios [15]. An approximate linearization method is developed to facilitate a rapid solution for ETP models in [16]. However, most existing research depends heavily on meteorological forecasts or observations from weather stations as external inputs for thermal simulations. On the one hand, meteorological forecast models are based on meteorological satellites to simulate mesoscale and large-scale temperature distributions (over 10km·10km) [17], which cannot capture microscale urban weather changes. On the other hand, weather stations, typically located in open spaces, fail to represent the realistic temperatures under the effects of wind resistance and reflection from man-made surfaces within urban building blocks [18]. Consequently, meteorological data cannot accurately reflect the temperature distribution around buildings, leading to an underestimation of the actual cooling demand.

The urban microclimate is influenced by the urban form, building geometry, land use, and human activities [19], reflecting climatic conditions in near-surface urban areas (1km·1km). With global warming and urbanization, the urban heat island (UHI) effect, a typical microclimate phenomenon, has garnered widespread attention [20]. On clear days, the scarcity of green spaces, heat reflection from man-made surfaces, and the wind resistance of buildings lead to significant heat accumulation within urban blocks [21]. As a result, the temperatures of both air and building surfaces are markedly higher than those recorded by weather stations. For now, the UHI effect has been documented in over 400 major cities worldwide [22], with the cooling electricity demand increasing up to 40% [23]. Regrettably, ACs, as the typical heat movers, generate cooling sources while emitting more waste heat into the surrounding environment, thereby exacerbating UHI [24]. In some typical cities, the waste heat emitted by ACs has increased the UHI intensity by more than 2°C [25]. Hence, there is a clear interaction between ACs usage and the surrounding microclimate.

Previous numerical models have been developed to simulate

the UHI effect and conduct experiments by isolating certain processes [26]. Masson *et al.* [27] propose an urban weather generator model to calculate the hourly air temperature and humidity based on weather data from meteorological stations. Then, the weather generator model is further expanded by Bueno *et al.* [28] into the rural station model, the vertical diffusion model, and the urban boundary layer model. To assess the impact of ACs utilization, a numerical simulation system has been established based on an urban thermal model [29]. The urban thermal model divides the temperature distribution at the block scale into the urban boundary layer, the urban canopy layer, and the urban surface layer [30]. Furthermore, Ohashi *et al.* [31] propose a numerical experiment using urban thermal model coupled with building energy model, which further extends to analyze the feedback mechanism on how the waste heat from ACs affects the microclimate. Additionally, an urban weather generator has been developed to calculate urban air temperatures using meteorological data from operational weather stations [32]. The above studies provide static numerical models to calculate the impact of ACs on microclimates. In practice, ACs adjust their operating power in real time based on user settings and demand response orders, indicating that the interactions are constantly evolving.

Therefore, further analysis is needed to understand the interactions between ACs and the microclimate, particularly focusing on their participation in demand response programs. This research is essential to fully capture the dynamic environmental impacts of ACs usage and optimize energy management strategies in urban settings. The major contributions of this paper are threefold:

- 1) We propose a unified thermal model integrated with ACs and urban microclimate to analyze the micro-scale heat flux transfer. This thermal model can quantify the interactions between extra energy demand of ACs and rising temperature of building blocks.
- 2) We formulate a two-stage optimal response capacity allocation model of ACs for providing peak-valley regulation services. Load aggregators (LAGs) engage in the cooperative game to maximize response benefits and implement SoC equalization to allocate capacity, enforcing consistent comfort levels for individual buildings.
- 3) Parametric equivalence and differential linearization methods are applied to efficiently solve and ensure the reliability of the optimal solution. A simplified benefit-sharing is employed to ensure the stability of the grand coalition.

We state our problem and introduce the unified thermal model in Section II. The two-stage response capacity allocation model is established in Section III. Numerical experiments are presented in Section IV. Section V concludes this paper.

II. UNIFIED THERMAL MODEL INTEGRATED WITH URBAN MICROCLIMATE AND AIR CONDITIONERS

This section presents a unified thermal model that integrates with urban microclimate and air conditioners (ACs), as illustrated in Fig. 1. In urban areas, heat fluxes from solar radiation and human activities accumulate at the block scale, driven by

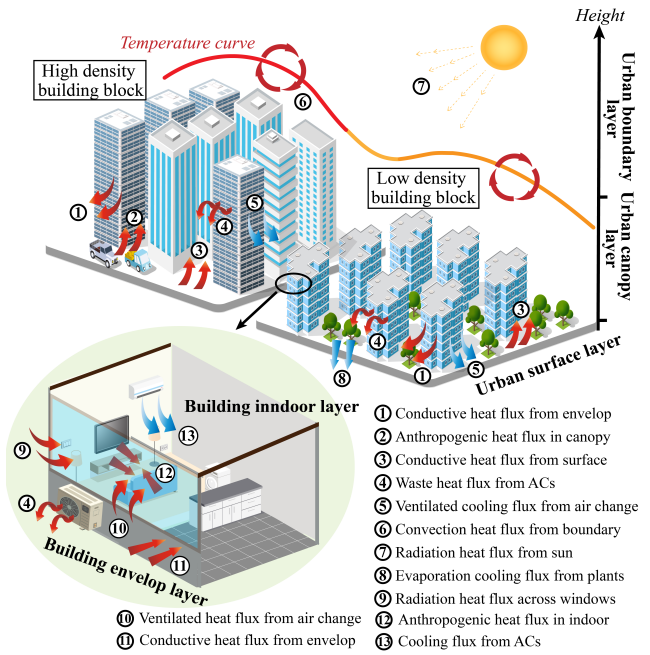


Fig. 1. The unified thermal model integrated with urban microclimate and air conditioners.

building wind resistance and surface reflections. For urban blocks with different underlying structures (e.g., building density, and vegetation cover), the accumulation of heat fluxes can vary and lead to microclimate changes. Consequently, it is crucial to categorize buildings into different microclimatic blocks based on their underlying structures.

For each classified block, we segment the urban microclimate into four vertical layers according to the validated urban thermal model: the urban surface layer, the urban canopy layer, the urban boundary layer, and the building envelope layer. Additionally, to quantitatively evaluate the interactions between building activities and the microclimate, we establish the following assumptions: The model's scope is limited to inner-city building blocks, and the simulated values are averaged across building blocks.

A. Urban Microclimate Model

1) *Urban Boundary Layer*: The urban boundary layer is the initial condition and upper boundary of urban canopy layer, typically encompassing a spatial scale larger than $5 \text{ km} \times 5 \text{ km}$. For neighboring building blocks, it is reasonable to assume that they share identical urban boundary layer conditions. In this study, the data of urban boundary layer is sourced from geostationary operational environmental satellites, specifically from the National Weather Science Data Centre [33].

2) *Urban Canopy Layer*: The urban canopy layer, defined as the space extending from ground level to 1.5 times height of buildings, is directly engaged with building energy activities. In microscale meteorological models (those with a diameter of less than 1 km), the temperature distribution within this layer is significantly influenced by the type of underlying surface, which impacts the transfer and accumulation of heat flux around buildings. For each building block, the urban canopy layer absorbs and accumulates both natural and anthropogenic

heat sources, and transfers heat flux with urban boundary layer, urban surface layer, and building envelope layer described as:

$$\begin{aligned} \rho_a c_a V_b^{uc} \frac{d\theta_{b,t}^{uc}}{dt} &= \rho_a c_a q_{b,t}^{ub} (\theta_{b,t}^{ub} - \theta_{b,t}^{uc}) \\ &+ \sum_{k \in \psi_{b,k}} \rho_a c_a q_{k,t}^{ve} (\theta_{k,t}^{in} - \theta_{b,t}^{uc}) + A_b^{\text{total}} Q_{b,t}^{eh} \\ &+ \sum_{k \in \psi_{b,k}} h_{b,t}^{ex} A_k^{en} (\theta_{k,t}^{en} - \theta_{b,t}^{uc}) + \sum_{k \in \psi_{b,k}} Q_{k,t}^{\text{waste}} \\ &+ h_{b,t}^{ex} A_b^{sur} (\theta_{b,t}^{sur} - \theta_{b,t}^{uc}), \quad \forall k \in \psi_{b,k}, b, t \end{aligned} \quad (1)$$

where t is the index of time; k is the index of buildings; b is the index of building blocks; ρ_a and c_a are the density and specific heat capacity of air, respectively; V_b^{uc} is the control volume of the urban canopy layer in block b ; $\theta_{b,t}^{uc}$, $\theta_{b,t}^{ub}$ and $\theta_{b,t}^{sur}$ are the temperature of urban canopy layer, urban boundary layer and urban surface layer, respectively; $\theta_{k,t}^{en}$ and $\theta_{k,t}^{in}$ are the temperature of building envelope layer and building indoor layer in building k , respectively; $q_{b,t}^{ub}$ is the airflow rate from urban boundary layer, described in (2); $q_{k,t}^{ve}$ is the ventilation rate from indoor, described in (3); $h_{b,t}^{ex}$ is the convective heat transfer coefficient between the external surface and the urban air, described in (4); A_k^{en} , A_b^{sur} and A_b^{total} are the building envelope areas, urban surface layer areas, and the total areas, respectively; $Q_{b,t}^{eh}$ is the average anthropogenic heat density of urban canopy layer; $Q_{k,t}^{\text{waste}}$ is the waste heat of ACs, described in (5); $\psi_{b,k}$ is index set of building k in block b .

The equation (1) shows the heat flux balance in the urban canopy layer. The remaining terms on the right-hand side represent the convective heat flux from the urban boundary layer, the convective heat flux from the building indoor, the anthropogenic heat flux, the conductive heat flux from the building envelope, the waste heat flux of ACs, and the conductive heat flux from the urban surface layer. The parameters calculation process is as follows [29], [32]:

$$q_{b,t}^{ub} = [(L_b - x_{0,b}) L_b] (1 - \lambda_{p,b}) U_{E,t} \quad (2)$$

$$q_{k,t}^{ve} = ACH_b \times A_{f,b} \times H_b \quad (3)$$

$$h_{b,t}^{ex} = 5.7 + 3.8U_{E,t} \quad (4)$$

$$Q_{k,t}^{\text{waste}} = \sum_{k \in \psi_{b,k}} (1 + COP_k) P_{k,t}^{ac} \quad (5)$$

where L_b is the averaging length scale; $x_{0,b}$ is the length scale of order; $\lambda_{p,b}$ is building plan area density; $U_{E,t}$ is the mean wind speed; ACH_b is the air change time; $A_{f,b}$ is the lateral area of heat exchange between the control volume and its surroundings; H_b is the average building height; COP_k and $P_{k,t}$ are the coefficient of performance and electricity power of ACs, respectively.

3) Urban Surface Layer: The urban surface layer refers to the upper surface to the depth having a constant temperature. For each building block, solar radiation is the primary heat source in the urban surface layer. However, due to the heat storage properties of artificial surfaces, the wind resistance of high-density buildings, and the lack of green spaces, the accumulated heat in the urban surface layer cannot be effectively

diffused, resulting in a continuous temperature rise. The heat transfer process between the urban surface layer and the urban canopy layer is described as follows:

$$\begin{aligned} \sum \rho_i c_i \Delta x_i A_{i,b}^{sur} \frac{d\theta_{b,t}^{sur}}{dt} &= (1 - \gamma_b) A_b^{sur} Q_{b,t}^{sun} \\ &+ K_r A_{r,b}^{sur} \frac{\bar{\theta}_{r,b}^{sur} - \theta_{b,t}^{sur}}{\Delta x_r} + K_v A_{v,b}^{sur} \frac{\bar{\theta}_{v,b}^{sur} - \theta_{b,t}^{sur}}{\Delta x_v} \\ &+ \sum_{k \in \psi_{b,t}} h_{b,t}^{ex} A_b^{sur} (\theta_{b,t}^{uc} - \theta_{b,t}^{sur}) - Q_{evp} A_{v,b}^{sur} \\ &- Q_{rad} A_b^{sur}, \quad \forall k \in \psi_{b,k}, b, t \end{aligned} \quad (6)$$

where $\sum \rho_i c_i \Delta x_i A_{i,b}^{sur}$ is the sum of the thermal mass of the urban surface layer; i is the index of surface types, including vegetated and man-made underlying surface; ρ_i and c_i are the density and heat capacity of surface i , respectively; Δx_i and $A_{i,b}^{sur}$ are the effective depth and area of surface i , respectively; γ_b is the albedo; $Q_{b,t}^{sun}$ is the solar radiation intensity; K_v and K_r are the conductivities of vegetated and man-made surfaces, respectively; $\bar{\theta}_{r,b}^{sur}$ and $\bar{\theta}_{v,b}^{sur}$ are the vegetated and man-made underlying temperatures at effective depth, respectively; Δx_v and Δx_r are the effective depth of vegetated and man-made surfaces, respectively; Q_{evp} and Q_{rad} are the transpiration heat flux and long-wave radiation heat flux to the sky, respectively. The remaining terms on the right-hand side represent solar insolation, the conductive heat flux of road and vegetated surfaces, the convective heat flux of urban canopy layer air, the evaporation heat flux, and the long-wave radiation heat flux.

4) Building Envelope Layer: The building envelope layer, encompassing walls and roofs, includes the control volume from the exterior to interior surface of buildings. Similar to the urban surface layer, the materials of building envelope layer are entirely man-made surfaces. The accumulation of solar heat flux in building envelope causes its temperature to be significantly higher than the surrounding air temperature. The heat transfer process among urban envelope layer, urban canopy layer, and building indoor layer is described as follows:

$$\begin{aligned} \rho_{en} c_{en} V_k^{en} \frac{d\theta_{k,t}^{en}}{dt} &= (1 - \alpha_k) \lambda_k A_k^{en} Q_{b,t}^{sun} \\ &+ h_{b,t}^{ex} A_k^{en} (\theta_{b,t}^{uc} - \theta_{k,t}^{en}) + U_k^{ei} A_k^{en} (\theta_{k,t}^{in} - \theta_{k,t}^{en}), \quad (7) \\ &\forall k \in \psi_{b,k}, b, t \end{aligned}$$

where ρ_{en} and c_{en} are the density and specific heat capacity of the building envelope, respectively; V_k^{en} is the control volume; α_k is albedo of the building envelope; λ_k is the percentage of effective sunlit area of the building envelop; U_k^{ei} is heat transfer coefficient between building indoor air and envelope. The remaining terms on the right-hand side represent solar insolation, convective heat flux of urban canopy layer, and convective heat flux of building indoor layer.

B. Air Conditioner Model

1) Building Indoor Layer: Air conditioners generate cooling to offset heat flux from ambient and anthropogenic heat flux, maintaining a set indoor temperature. The heat flux

balance at the building indoor layer is described as follows:

$$\rho_a c_a V_k^{in} \frac{d\theta_{k,t}^{in}}{dt} = U_k^{ei} A_k^{en} (\theta_{k,t}^{en} - \theta_{k,t}^{in}) + \beta_k A_k^{win} Q_{b,t}^{sun} + \rho_a c_a q_{k,t}^{ve} (\theta_{b,t}^{uc} - \theta_{k,t}^{in}) + N_k^{\text{floor}} A_k^{in} Q_{k,t}^{ih} - Q_{k,t}^{\text{cool}}, \forall k \in \psi_{b,k}, b, t \quad (8)$$

$$Q_{k,t}^{\text{cool}} = COP_k P_{k,t}^{ac}, \forall k, t \quad (9)$$

where V_k^{in} is the indoor control volume of building k ; β_k is the sunlight transmission coefficient of windows; A_k^{win} is the window area of building k ; N_k^{floor} is the number of floors; A_k^{in} is the floor area; $Q_{k,t}^{ih}$ is the indoor anthropogenic heat density; $Q_{k,t}^{\text{cool}}$ is the cooling flux generation by air conditioners. The remaining terms on the right-hand side represent the convective heat flux of building envelop, the radiation heat flux of the sun across the window, the ventilated heat flux from air change required, the anthropogenic heat flux from indoor human activities, and the cooling supply from air conditioners.

2) *Virtual Energy Storage Model*: The thermal inertia of building materials plays a critical role in moderating indoor temperature fluctuations. This property gives the building a virtual storage capacity [34], which ensures that short-term adjustments in air conditioner settings do not result in significant temperature changes. Humans typically have limited sensitivity to minor fluctuations in indoor temperature, which allows for a broader range of adjustability in air conditioner settings. Therefore, the virtual storage capacity of building is related to the minimum and maximum temperatures acceptable to indoor users. Assume that the user's comfort zone is $[\theta_k^{in,\min}, \theta_k^{in,\max}]$, the building's stored energy is 0 at room temperature $\theta_k^{in,\max}$, and the building is filled at room temperature $\theta_k^{in,\min}$. Hence, the virtual storage capacity for each building can be described as (10) and the state of charge (SoC) is described as (11):

$$E_k^{\max} = \rho_a c_a V_k^{in} (\theta_k^{in,\max} - \theta_k^{in,\min}) \quad (10)$$

$$SoC_{k,t} = \frac{E_{k,t}}{E_k^{\max}} = \frac{\theta_k^{in,\max} - \theta_{k,t}^{in}}{\theta_k^{in,\max} - \theta_k^{in,\min}} \quad (11)$$

where $E_{k,t}$ is virtual storage capacity of building k at time t ; E_k^{\max} is the maximum storage capacity; $\theta_{k,t}^{in,\min}$ and $\theta_k^{in,\max}$ are the lower and upper temperature limits for user comfort, respectively; $SoC_{k,t}$ is the state of charge of building k .

III. TWO-STAGE OPTIMAL RESPONSE CAPACITY ALLOCATION OF AIR CONDITIONERS

Section II illustrates a dynamic interaction that building energy activities affect the surrounding microclimate conditions, while the microclimate changes simultaneously impact buildings. Specifically, air conditioners are the root of this interaction, generating cooling air while emitting large amounts of waste heat into surrounding environment. Simultaneously, the power consumption of air conditioners exhibits distinct peak-valley characteristics following the ambient temperature changes during the day. Hence, we can regulate the power consumption of air conditioners in different periods for two

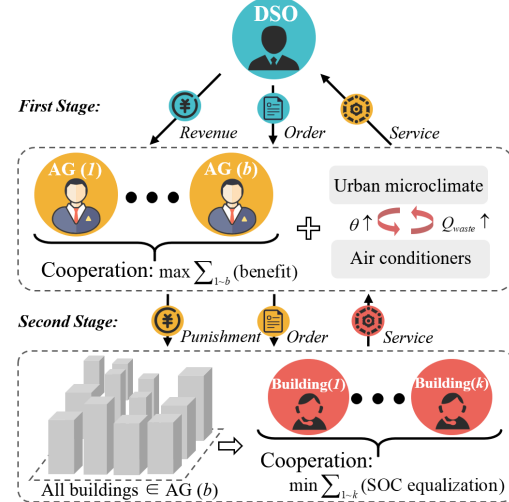


Fig. 2. The structure of two-stage capacity allocation optimization model.

main objectives, i.e., mitigating adverse impacts on microclimate and assisting the power system stable operation. Here, our focus on system stable operation refers to smoothing the peak-to-valley difference of air conditioner loads, by utilizing building thermal inertia and user-adjustable comfort intervals. The proposed unified thermal model is implemented in the building capacity allocation process, considering the interaction effects at both the building block and individual levels. Fig. 2 depicts the structure of proposed two-stage response capacity allocation optimization model. The participants in completing the response include the distribution system operator (DSO) who distributes the total response demand, the load aggregators (LAGs) who manage the block buildings, and the individual buildings who perform the response capacity.

The DSO allocates up- or down-regulation demand capacity based on the total load profile. In the conventional scenario, the DSO allocates the response capacity based on the load share of LAGs, who are individuals with independent revenue. However, due to the underlying differences in blocks, the same share of response capacity will result in different microclimate consequences during response implementation. In particular, for high-density building blocks, participation in upward response at midday will severely worsen microclimate temperatures. Thus, *in the first stage*, we propose an optimal allocation strategy between LAGs, considering the interaction between buildings and the surrounding microclimate. The cooperative objection is to maximize social welfare and mitigate urban microclimate deterioration. Then, *in the second stage*, each LAG allocates response capacity to all managed building individuals based on the optimized result of the first stage. In this process, the conventional method of allocating according to the average response power density will cause under- or over-regulation of some buildings due to the differences in individual building structures. To address this issue, we propose an optimal allocation based on SoC equalization to ensure the fairness of response among individual buildings.

A. First-Stage Optimization: Allocation Among LAGs

To achieve the simultaneous solution of large-scale urban building clusters, we propose the parametric equivalence to compute building block averages in the first-stage optimization model. There are two main points: (1) First, each block only

needs to obtain the total adjustable capacity of all managed buildings. And the generated waste heat by the same response capacity is constant regardless of how it is distributed; (2) Based on the building indoor layer model, the energy consumption density only depends on the surrounding microclimate conditions, and buildings within the same blocks have the same microclimate conditions. Therefore, it is effective to apply the average parameter values of buildings within the same blocks, ignoring the individual differences.

1) *Objective*: The objective function is to maximize overall social welfare, and the various costs include the revenue of participating in the DSO response, penalties for building indoor temperature deviations, and penalties for worsening urban temperatures, described as follows:

$$\max F_1 = \sum_{t \in T} \sum_{b \in B} [F^{DR} - F^{in} - F^{uc}] \quad (12)$$

$$F^{DR} = \alpha_1 |N_b \bar{P}_{b,t}^{ac} - P_{b,t}^{ac,basic}| \Delta t \quad (13)$$

$$F^{in} = \alpha_2 \bar{N}_k^{\text{floor}} \bar{A}_k^{in} N_b |\bar{\theta}_{b,t}^{in} - \theta^{in,basic}| \Delta t \quad (14)$$

$$F^{uc} = \alpha_3 A_b^{\text{total}} (\theta_{b,t}^{uc} - \theta_{b,t}^{uc,basic}) \Delta t \quad (15)$$

where T and B are the index set of time and block, respectively; F^{DR} , F^{in} and F^{uc} are the revenue of participating in the DSO response, penalties for building indoor temperature deviations, and penalties for worsening urban temperatures, respectively; α_1 , α_2 and α_3 are the cost factors, respectively; N_b is the number of buildings; $\bar{P}_{b,t}^{ac}$ is the average power of ACs; $P_{b,t}^{ac,basic}$ is the baseline power before demand response; $\theta^{in,basic}$ is the baseline indoor temperature before demand response, which is user expected temperature; \bar{N}_k^{floor} and \bar{A}_k^{in} are the average number of floor and floor area of all buildings, respectively; $\theta_{b,t}^{uc,basic}$ is the baseline temperature of urban canopy layer before demand response; Δt is time step.

2) *Constraints*: The modeling constraints in the first stage include urban microclimate modeling constraints (1), (6) and (7), and ACs constraints (8). Based on the above equivalent analysis, the building waste heat $\sum_{k \in \psi_{b,k}} Q_{k,t}^{\text{waste}}$ in (1) can be replaced by $\bar{N}_b \bar{P}_{b,t}^{ac} (1 + COP_b)$. The heat flux between urban canopy layer and building envelop layer $\sum_{k \in \psi_{b,k}} h_{b,t}^{ex} A_k^{en} (\theta_{k,t}^{en} - \theta_{b,t}^{uc})$ can be replaced by $\bar{N}_b \bar{A}_k^{en} h_{b,t}^{ex} (\bar{\theta}_{b,t}^{en} - \theta_{b,t}^{uc})$. Besides, the model contains total response capacity constraints (16), ACs operating power constraints (17), and indoor comfort constraints (18), can be described as follows:

$$DR_t^{\min} \leq \sum_{b \in B} |N_b \bar{P}_{b,t}^{ac} - P_{b,t}^{ac,basic}| \leq DR_t^{\max}, \forall t \quad (16)$$

$$\bar{P}_b^{ac,\min} \leq \bar{P}_{b,t}^{ac} \leq \bar{P}_b^{ac,\max}, \forall b, t \quad (17)$$

$$\theta^{in,\min} \leq \bar{\theta}_{b,t}^{in} \leq \theta^{in,\max}, \forall b, t \quad (18)$$

where DR_t^{\min} and DR_t^{\max} are the lower and upper limits of total response capacity of the DSO, respectively; $\bar{P}_b^{ac,\min}$ and $\bar{P}_b^{ac,\max}$ are lower and upper limits of ACs power, respectively.

3) *Benefit-Sharing Scheme*: A typical cooperative game is characterized by the set of players, the value function

which quantifies the worth of the coalition, and a benefit-or cost-sharing scheme satisfying all players [35]. In our cooperative, the set of players \mathcal{N} are all building aggregators participating in the demand response, and the value function v is the demand benefit in (12). Hence, we can define a set of coalition as $G = (\mathcal{N}, v)$, $\mathcal{N} \in \mathbb{R}$. In the non-cooperative pattern, the building aggregators can only passively execute the response capacity demand of DSO and receive a fixed response benefit. On this occasion, the total benefit can be described as $\sum_{i \in \mathcal{N}} v_i$ (nco). Conversely, in the cooperation pattern, the response capacity of the building aggregators participating in the grand coalition is reallocated and the total benefit can be described as $v_{\mathcal{N}}$ (co).

In the proposed model, the benefit contains response revenue, ambient temperature deterioration penalty, and indoor comfort deviation penalty. Due to the differences in urban microclimate and building interactions between blocks, building aggregators will always proactively engage in the grand coalitions to redistribute response capacity, which means shifting the response impact and reducing the penalty cost. Therefore, the value function is superadditive and for all disjoint set $\mathcal{S}, \mathcal{T} \subseteq \mathcal{N}$, satisfying $v(\mathcal{S} \cup \mathcal{T}) \geq v(\mathcal{S}) + v(\mathcal{T})$.

A proper benefit-sharing scheme is the crucial key to ensuring the stability of the grand coalition. In the cooperative game, x_i is a set of payoff allocations for player i . Then, the core $\mathcal{C}(v)$ is defined as the set of payoff vectors under which no coalition has a value greater than the sum of its members' payoffs [36], described as:

$$\mathcal{C}(v) = \left\{ x \in \mathbb{R} : \sum_{i \in \mathcal{N}} x_i = v(\mathcal{N}); \sum_{i \in \mathcal{S}} x_i \geq v(\mathcal{S}), \forall \mathcal{S} \subseteq \mathcal{N} \right\} \quad (19)$$

As the value function is superadditive, the proposed cooperative game is convex. The core of a convex game is non-empty, and since any subgame of a convex game is convex, the core of any subgame is also non-empty. The Shapley Value [37] is a widely accepted method for the benefit-sharing scheme in a convex game, described as :

$$x_i = \sum_{\mathcal{S} \subseteq \mathcal{N} \setminus \{i\}} \frac{|\mathcal{S}|!(|\mathcal{N}| - |\mathcal{S}| - 1)!}{|\mathcal{N}|!} [v(\mathcal{S} \cup \{i\}) - v(\mathcal{S})] \quad (20)$$

The Shapley Value focuses on analyzing the marginal contributions of each player to possible coalitions. For a game with i players, the number of non-empty coalitions would be $2^i - 1$. As the number of players increases, the computational complexity of the Shapley Value becomes exceptionally high. Therefore, we adopted a simplified benefit allocation approach [38] based on the above characteristics of the proposed game.

First, the incremental benefit $O_{\mathcal{N}}$ from the grand coalition (co) compared to non-cooperative pattern (nco) is as follow:

$$O_{\mathcal{N}} = v(\text{co}) - \sum_{i \in \mathcal{N}} v_i(\text{nco}) \quad (21)$$

Then, the marginal contributions of each player i to the

grand coalition can be described as:

$$\mathcal{O}_i = v_{\mathcal{N}}(\text{co}) - v_{\mathcal{N}/i}(\text{co}) - \sum_{i \in \mathcal{N}} v_i(\text{nco}) \quad (22)$$

We define the contribution weight $\lambda_i = \mathcal{O}_i / \sum_{i \in \mathcal{N}} \mathcal{O}_{\mathcal{N}}$, and take it into the marginal contribution equation, the benefit gained by player i can be described as:

$$v_i(\text{co}) = v_i(\text{nco}) + \lambda_i \mathcal{O}_i \quad (23)$$

Based on the simplified benefit-sharing scheme, the set of non-empty coalitions is reduced to i in a cooperative game involving i players. It is crucial to emphasize that the stability of this scheme ensures that all LAGs are willing to participate in the grand coalition managed by the DSO.

B. Second-Stage Optimization: SoC Equalization

The building's virtual energy storage capacity allows for brief adjustments to ACs, ensuring that indoor temperatures remain within a comfortable range. The SoC of an individual building is defined in (11). Following the first-stage allocation result, LAGs are tasked with distributing the total response duty across all managed buildings. This distribution process needs to consider the varying response characteristics of each building, which arise from the distinct geometric properties of individual buildings. Hence, the second-stage optimization is formulated as follows:

1) *Objective*: Minimizing the SoC variance of k buildings in b LAGs, described as follow:

$$\min F_2 = \sum_{t \in T} \sum_{k \in \psi_{b,k}} \left[\text{SoC}_{k,t}^2 - \bar{\text{SoC}}_{t,b}^2 \right] \quad (24)$$

$$\bar{\text{SoC}}_{t,b} = \frac{1}{k} \sum_{k \in \psi_{b,k}} \text{SoC}_{k,t}, \forall t, b \quad (25)$$

where T is the index set of time; $\bar{\text{SoC}}_{t,b}$ is the average SoC of all buildings in block b .

2) *Constraints*: In the second stage, the ACs operation in each building block complies with constraints (8) and (9). Specifically, the microclimate parameters for the blocks, including building envelope temperature $\bar{\theta}_{b,t}^{en}$ and urban canopy temperature $\theta_{b,t}^{uc}$, are determined by the first stage. Besides, the total response of all buildings in the blocks satisfies the response scheme in the first stage as:

$$\sum_{k \in \psi_{b,k}} \left(P_{k,t}^{ac} - P_{k,t}^{ac,basic} \right) = N_b \bar{P}_{b,t}^{ac} - P_{b,t}^{ac,basic}, \forall b, t \quad (26)$$

For individual buildings, the ACs operation satisfies the power capacity constraint, and the virtual energy storage satisfies the SoC constraint, described as follows:

$$P_k^{ac,min} \leq P_{k,t}^{ac} \leq P_k^{ac,max}, \forall k, t \quad (27)$$

$$\text{SoC}_k^{\min} \leq \text{SoC}_{k,t} \leq \text{SoC}_k^{\max}, \forall k, t \quad (28)$$

where $P_k^{ac,min}$ and $P_k^{ac,max}$ are the lower and upper limits of ACs power in building k , respectively; SoC_k^{\min} and SoC_k^{\max} are the lower and upper limits of SoC, respectively.

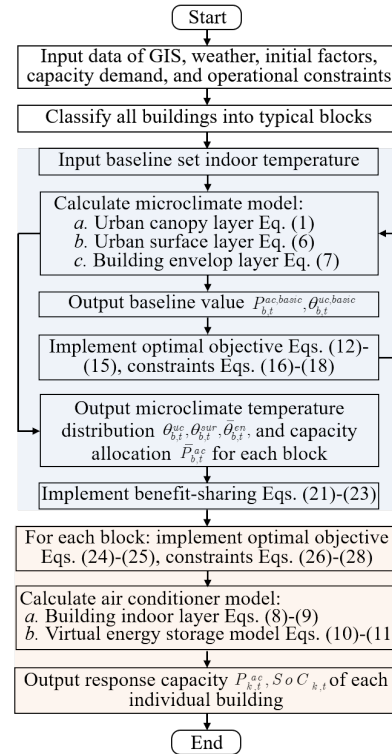


Fig. 3. Solving step flowchart of the proposed two-stage optimization model.

C. Differential Linearization

To improve the solution efficiency, the differential linearization method is employed to transform the first-order differential equations to linearized constraints. First, we provide the equivalent thermal parameters model for each layer, described as follows:

$$C \frac{d\theta^{\chi_2}(t)}{dt} = R [\theta^{\chi_1} - \theta^{\chi_2}] + Q(t), t \in [0, T] \quad (29)$$

where C is the equivalent heat capacity; R is the equivalent thermal resistance; $\theta^{\chi_2}(t)$ is the calculated temperature of the target layer at time t ; $\theta^{\chi_1}(t)$ is the temperature of layers associated with target layer; $[0, T]$ is the optimization period.

Take $\Delta\tau = \frac{\Delta t}{N}$, for each time t_m in Δt can be described as follows:

$$\frac{d\theta^{\chi}(t_m)}{dt} = \frac{\theta^{\chi}(t_m + \Delta\tau) - \theta^{\chi}(t_m)}{\Delta\tau}, t_m \in [t_I, t_{II}] \quad (30)$$

Further, the computational procedure of $\theta^{\chi}(t_m)$ can be differential linearized as follows:

$$\begin{aligned} \theta^{\chi_2}(t_I + \Delta\tau) &= \frac{R\Delta\tau}{C} [\theta^{\chi_1}(t_I) - \theta^{\chi_2}(t_I)] \\ &+ \frac{\Delta\tau}{C} Q(t_I) + \theta^{\chi_2}(t_I) \\ &\dots \end{aligned}$$

$$\begin{aligned} \theta^{\chi_2}(t_m : t_I + m\Delta\tau) &= \frac{R\Delta\tau}{C} [\theta^{\chi_1}(t_I) - \theta^{\chi_2}(t_I + (m-1)\Delta\tau)] \\ &+ \frac{\Delta\tau}{C} Q(t_I) + \theta^{\chi_2}(t_I + (m-1)\Delta\tau) \end{aligned} \quad (31)$$

where $\Delta\tau$ is the calculation step; $\Delta t = t_{II} - t_I$ is the optimization step; N is the number of differentials.

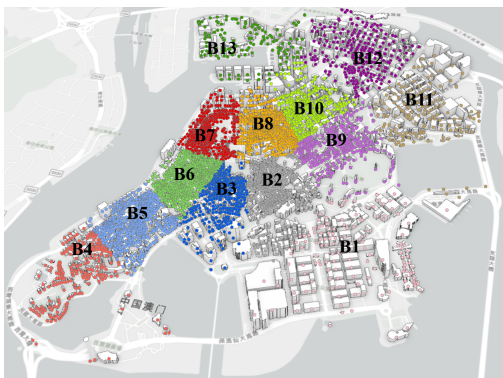


Fig. 4. Case simulation in Macau peninsula with 13 blocks.

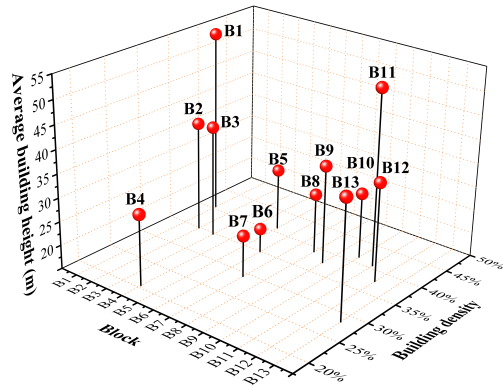


Fig. 5. The distribution of building density and average height.

D. Solving Step

This paper proposes a two-stage capacity allocation optimization model considering the interaction with surrounding urban microclimate, and the solving steps are illustrated in Fig. 3. Following data input and initialization, the first stage involves the cooperative optimal allocation of AGs to minimize total operational costs. Subsequently, the results from the first stage, including capacity and microclimate temperature distribution, are utilized in the second-stage optimization. In this stage, the building-individual capacity allocation is executed for each block based on SoC equalization, ensuring response fairness. Upon completion of the two-stage optimization, the total response capacity of the DSO is efficiently allocated to each individual building.

IV. CASE STUDIES

The Guangdong-Hong Kong-Macao Greater Bay Area is the most typical high-temperature and high-humidity region in China, characterized by densely distributed buildings that intensify urban microclimate phenomena. Based on the building GIS data (data from the Institute of Geographic Sciences and Natural Resources Research, CAS) [39], we select all 4,739 individual buildings in the Macau Peninsula as test cases. The data of the urban boundary layer is from the geostationary operational environmental satellite (data from the National Weather Science Data Centre) [33], which is the initial condition and upper boundary of the canopy layer. The parameter settings are shown in Table I.

The determining factor for the interaction of buildings with the surrounding microclimate is the spatial distribution of the building. Based on the ArcGIS tool, we calculate the

TABLE I
PARAMETER SETTINGS OF MICROCLIMATE MODEL

Items	Settings
Air specific heat capacity and density	1006J/kg·°C; 1.29 kg/m ³
Convective heat transfer coefficient	1.5W/m ³ ·K
Canopy anthropogenic heat density	30 W/m ²
Indoor anthropogenic heat density	10 W/m ²
Air change time	0.5h ⁻¹
Coefficient of performance	3.6
Density and depth of external surface	800 kg/m ³ ; 0.4m
Underlying temperatures and albedo	20°C; 0.2
Sunlight coefficient and floor height	0.3; 3m
Time-step and baseline temperature	600s; 24°C

geometric centers of the buildings on the Macau Peninsula. Subsequently, the Density Clustering Toolkit is employed to classify these buildings into 13 typical blocks, as illustrated in Fig. 4. Additionally, the distribution of building density and average height across these blocks is depicted in Fig. 5.

A. Interaction Analysis of ACs in Buildings with Surrounding Microclimate

Case 1: Baseline ACs' operation without considering the interaction with urban microclimate.

Case 2: Baseline ACs' operation considering the interaction with urban microclimate.

Increased urban building density results in higher wind resistance and enhanced reflection of heat flux, thereby contributing to the accumulation of anthropogenic heat and solar radiation within urban blocks. We present a detailed comparative analysis of the microclimate temperature distribution before and after the interactive operation in Fig. 6, including the low-density building block B4 and the high-density building block B11.

In Case 1 independent operation, the comparison between Fig. 6(a) and Fig. 6(b) highlights that the rise in building density accounts for a temperature differential of 1.1°C in the urban canopy between B4 and B11. Notably, the impact of increased building density is more pronounced at the building envelope layers, as depicted in Fig. 6(c) and Fig. 6(d). At 15:00, the temperature disparity between the building envelope layers of B4 and B11 peaks at 3.92°C.

In independent operations, solar radiation is the predominant source of urban heat. However, with the widespread adoption of ACs, a substantial amount of indoor heat is expelled into the surrounding environment through these units, representing a significant additional heat source. This effect is particularly pronounced in areas with high-density building blocks. The elevated urban temperatures lead to increased AC usage, thereby generating more waste heat in the vicinity of the buildings. In other words, there is a vicious cycle between ACs energy consumption and urban temperatures. For instance, in Case 2, as illustrated in Fig. 6(b) and Fig. 6(d), the interaction involving ACs increased 2.96°C in the maximum urban canopy temperature and a 2.81°C rise in the maximum building envelope temperature. Furthermore, we present the distribution of temperature increases across the urban canopy for all 13 blocks in Fig. 7. Notably, Blocks B11 and B5, which feature high-density buildings, exhibit the most substantial temperature increases, whereas Blocks

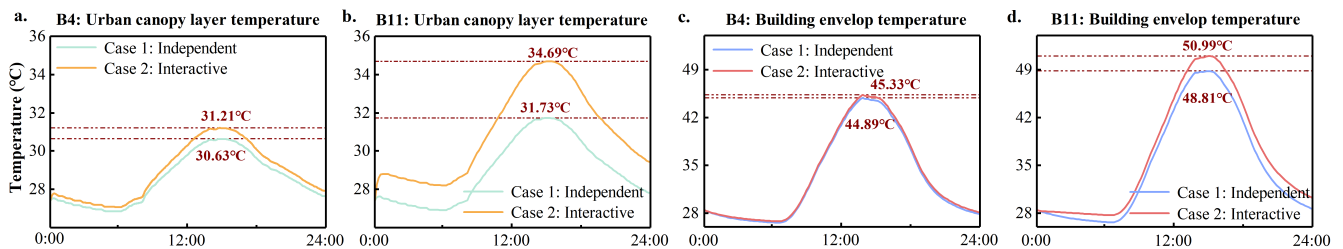


Fig. 6. Temperature distribution differences between Case 1 and Case 2 in B4, B11.

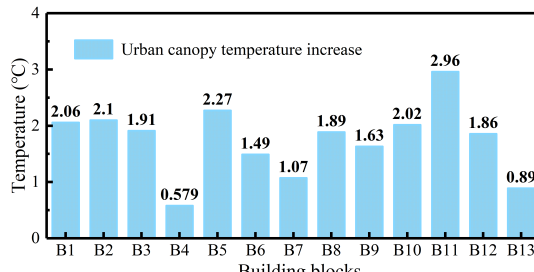


Fig. 7. Maximum temperature increase between Case 1 and Case 2 in 13 blocks.

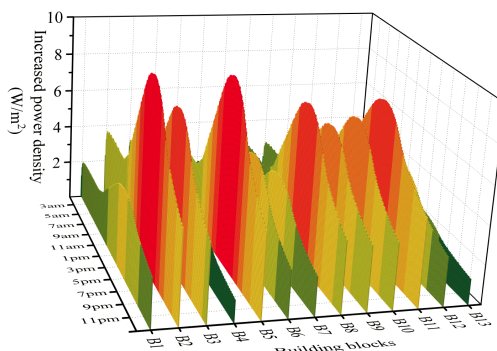


Fig. 8. The increased power density distribution in Case 2 in 13 blocks.

B4 and B13, characterized by low-density buildings, show the least significant increases. The key reason is that high-density buildings emit more waste heat and the wind resistance effect prevents the diffusion of the waste heat. We calculate the Pearson correlation coefficient r of 0.87 between temperature increase x and building density y based on (32), which further indicates that building density is a crucial factor influencing the interaction between ACs and urban microclimate.

$$r = \frac{\sum (x_i - \bar{x})(y_i - \bar{y})}{\sqrt{\sum (x_i - \bar{x})^2 \sum (y_i - \bar{y})^2}} \quad (32)$$

The above analysis underscores the significant impact of interactive operations on the urban microclimate. Indeed, in this vicious cycle, the energy consumption of ACs equally increases with stronger interactions. As the urban canopy temperature and the building envelope temperature rise, the heat exchange between the building and its surrounding microclimate intensifies, compelling the ACs to work harder to maintain indoor comfort. Fig. 8 illustrates the distribution of the increased energy density after considering the interaction between ACs and surrounding microclimate in Case 2. Notably, the increase in energy consumption due to this interaction is more pronounced during midday hours across all blocks and diminishes as the urban temperature decreases. Furthermore, this increase is more severe in high-density building blocks such as B2, B3, B5, B8, and B11. Fig. 9 reveals that in the high-density block B11, the maximum

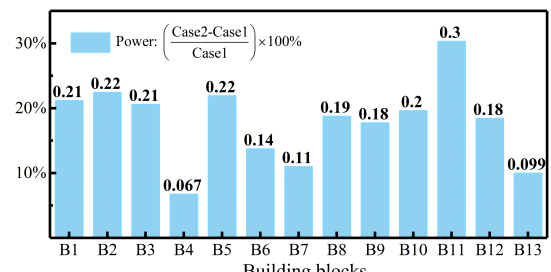


Fig. 9. The power density increase between Case 1 and Case 2 in 13 blocks.

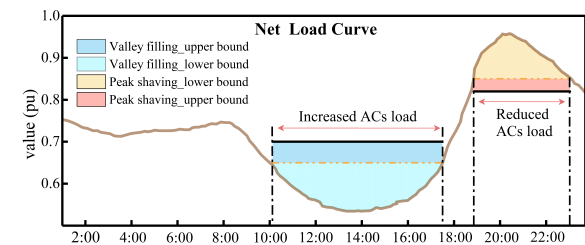


Fig. 10. Total demand response capacity of DSO.

increase in building energy consumption due to interaction has surpassed 30%. This indicates that in urban areas with dense buildings, it becomes challenging to effectively disperse the waste heat emitted by ACs, making it a critical factor in escalating ACs energy consumption.

B. First-Stage Response Capacity Allocation: Cooperation Analysis Among Urban Blocks

Case 3: Building blocks participate independently in demand response based on Case 2.

Case 4: Building blocks participate collaboratively in demand response based on Case 2.

In Case 2, we established the indoor temperature at a baseline of 24°C to evaluate the interaction between ACs and urban microclimate. This scenario reflects the ACs baseline load before demand response. In the demand response scenario, we anticipate a future with a high penetration of decentralized photovoltaic, resulting in a “duck curve”, as shown in Fig. 10. This phenomenon occurs when solar energy production peaks at midday and drops sharply in the evening, leading to significant variations in net load. Then, the DSO orders an upward or downward adjustment based on the net load curve and the LAGs participate in demand response based on the load baseline and adjustable capacity. In Case 3, individual blocks respond to demand according to their proportionate share of the load, adhering to the regulation curves depicted in Fig. 10. In Case 4, all blocks cooperate to fulfill the regulation demand for the whole Macau Peninsula.

In subsection IV-A, we reveal a vicious circle that exists between buildings and surrounding microclimate, and the intensity is strongly associated with the building density.

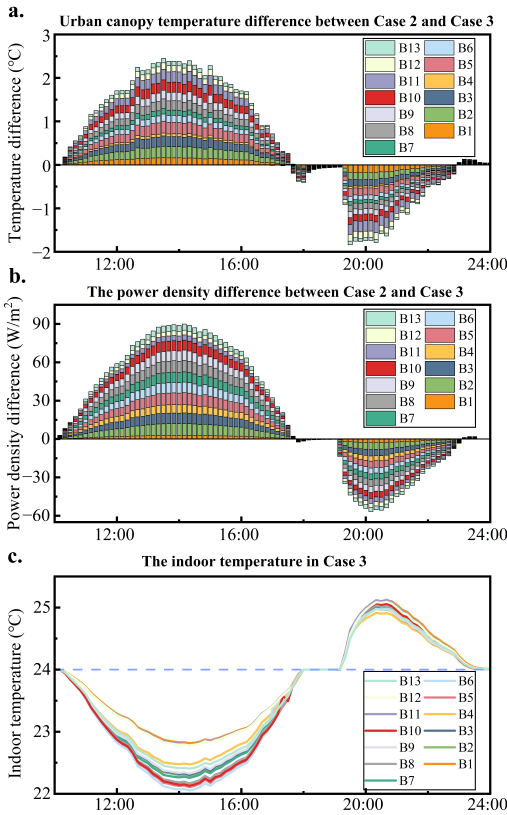


Fig. 11. Independent demand response results in Case 3.

Specifically, in areas with high building density, the increased use of air conditioners at midday releases substantial waste heat, thereby worsening ambient temperatures and damaging indoor comfort. Therefore, in the proposed cooperative game with maximizing profit, LAGs will actively seek cooperation to mitigate this vicious cycle. Detailed comparisons of scenarios before and after cooperation are presented in Case 3 and Case 4, respectively.

The independent demand response results in Case 3 are illustrated in Fig. 11. First, the participation of buildings in demand response programs significantly affects urban canopy temperatures. During the up-regulation stage, the ACs power increase results in the canopy temperature rise, peaking at 13:30, as depicted in Fig. 11(a). The average temperature increase across the 13 building blocks is 0.188°C , with blocks B2, B3, B5, B8, B9, B10, and B11 experiencing above-average increases. Notably, the high-density block B5 shows the most significant vicious circle, with a temperature increase exceeding 0.27°C . Correspondingly, the low-density block B4 experiences minimal impact from demand-responsive regulations, with a peak of only 0.067°C . The primary reason for the above disparity is that differences in building density lead to different rates of diffusion of ACs waste heat. The high density of the building stock leads to a continuous accumulation of waste heat within the block.

Then, Fig. 11(b) depicts the change in power density of the building blocks in demand response programs. Comparing Fig. 11(a) and Fig. 11(b) reveals two key phenomena: on the one hand, there is the same trend between change in urban canopy temperature and regulation of ACs. On the other hand, the temperature rise induced by the ACs is varying across the 13 blocks. Among them, B11 implements a maximum

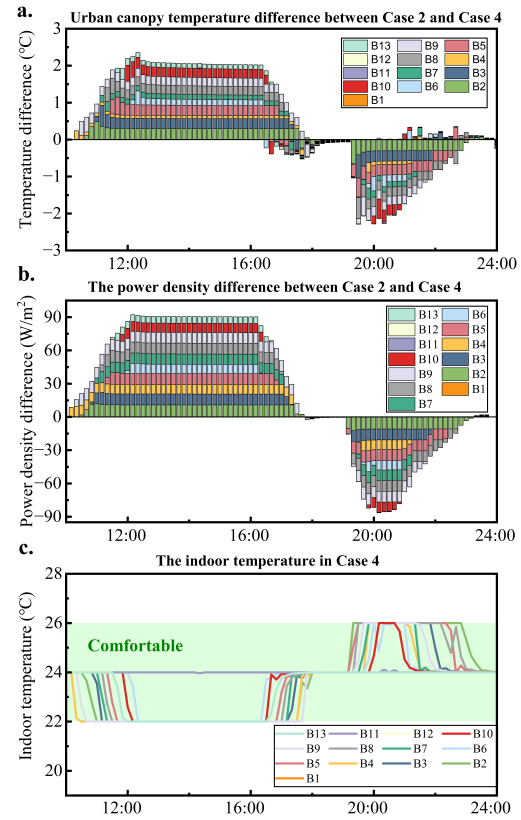


Fig. 12. Cooperative demand response results in Case 4.

up-regulation power density of 4.08W/m^2 , which is much lower than the average of 6.92W/m^2 . However, B4 experiences the second highest temperature rise of 0.24°C after B5. On the contrary, B4 implements a significantly higher maximum up-regulation power density of 6.59W/m^2 , registering only a temperature rise of 0.067°C . The above analysis shows that the interaction between the ACs and the surrounding microclimate cannot be ignored when the ACs are involved in the demand response process. Due to the differences in the underlying, the same amount of response will also have different consequences in blocks, directly forcing the LAGs to pay different penalty costs. To improve the global benefits and mitigate the impacts on the urban microclimate, we implement the proposed first-stage capacity allocation scheme in Case 4.

In the grand coalition, the total demand from the DSO is reallocated among LAGs to alleviate adverse effects on both outdoor microclimate and indoor comfort. Fig. 12(a) illustrates the temperature deviations for each building block in the cooperative demand response scenario compared to the baseline scenario. It can be seen that the canopy temperature rise resulting from the midday up-regulation response is effectively mitigated. In the down-regulation stage, the canopy temperature of all blocks decreases as well. This result stems from redistributing the response capacity from blocks with significant interactions to those with minimal, thus preventing excessive temperature rises in certain blocks, such as B11. Besides, Fig. 12(b) depicts the optimized scheduling scheme after all building blocks cooperatively participate in demand response. During the up-regulation stage, a comparison of power densities shows that blocks B1, B2, and B12 scarcely engage in the response process. On the contrary, the response densities of B4 and B9 increase significantly contrasting Fig.

TABLE II
PROFIT-SHARING SCHEME IN CASE 4 (*10³ CNY)

Case	B1	B2	B3	B4	B5	B6	B7	B8	B9	B10	B11	B12	B13
Independent	8.94	34.71	22.85	9.54	15.82	4.55	9.07	16.89	26.25	13.97	20.40	8.63	13.83
Cooperation	17.22	46.54	30.34	12.98	20.58	5.99	11.93	22.11	35.29	18.23	28.22	13.25	18.66

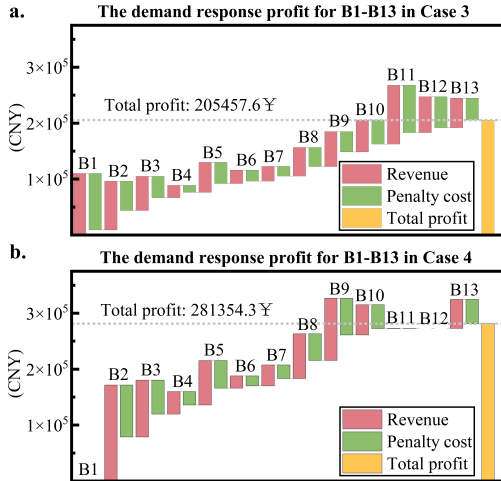


Fig. 13. Profit Comparison of 13 blocks.

11(b). In the down-regulation stage, a similar pattern of regulation is observed. The comparison between Fig. 11(c) and Fig. 12(c) reveals that all blocks exhibit similar indoor temperature changes during the independent response process. Additionally, blocks that achieve higher profit through cooperation are allocated greater response capacities. This arrangement ensures that the benefits of cooperation are maximized by leveraging the response potential of each block effectively.

Fig. 13 depicts the profit comparison of independent and cooperative participation in response to the 13 blocks. It can be seen that the underlying difference leads to differences in the net profit in Fig. 13(a), primarily due to differing microclimate interactions. In the independent response scenario, despite having the most response capacity, B1 and B11 exhibit the lowest net profit. Conversely, in the cooperative scenario, response capacity is reallocated to leverage the potential for inter-block cooperation. Fig. 13(b) shows that blocks with higher net profit, such as B2 and B9, are prioritized for response activities. This strategic reallocation of response capacity leads to an overall increase in total benefits by 36.94%, demonstrating the efficiency of optimized cooperative strategies.

In the first stage of response capacity allocation, participation in the grand coalition between blocks maximizes total profit. However, a prerequisite for ensuring the stability of the grand coalition is that each LAG can achieve more profit after cooperation. Hence, we implement the proposed profit allocation strategy in Case 4. The gains of each LAG before and after participating in the grand coalition are shown in Table II. On the one hand, based on our proposed simplified cooperation profit-sharing scheme, all LAGs participating in the grand coalition have increased their profit. On the other hand, it can be noted that even though B1 is not assigned a response task, B1's profit increases the most after cooperation as a result of its large marginal contribution. On the contrary, B6 has almost no change in its corresponding task before and after the cooperation, and therefore has the smallest marginal

profit from the cooperation.

C. Second-Stage Response Capacity Allocation: Individual Satisfaction Considering Differences in Building Capacities

Case 5: Allocate to each building based on response density of the first-stage allocation.

Case 6: Allocate to each building based on SoC equilibrium.

In the second stage, each LAG performs response capacity allocation to all managed buildings. Traditionally, the response tasks are assigned based on the average demand response density, as specified in Case 5. In this method, the response capacity of each individual building is determined by the demand response density and the total indoor area. However, while this allocation considers the variability of the buildings' adjustable capacity, it ignores the interaction between the buildings and surrounding microclimate. To ensure fairness and comfort in performing demand response for all buildings, we perform the optimization of response capacity allocation based on SoC equalization in Case 6.

Detailed comparative analyses are provided in B3, as shown in Fig. 14. First, the demand response density curve from first-stage allocation is depicted in Fig. 14(a), which is executed in individual buildings in Case 5. Observations indicate that post-demand response implementation, some buildings experience indoor temperatures outside the comfort zone, suggesting an exceedance of their adjustable capacity, as depicted in Fig. 14(c). This issue primarily arises due to the varying geometries of buildings in each block. Buildings with a higher proportion of peripheral area are more exposed to microclimate influences and exhibit reduced virtual energy storage capacity. Subsequently, we redistribute the demand response density to accommodate the distinct characteristics of each building, depicted in Fig. 14(b). This optimized approach ensures that the indoor temperatures of all 259 buildings in Block B3 maintain a uniform operational profile, remaining within the designated comfort zone.

To further validate the effectiveness of proposed strategy, the response process analysis in B10 is depicted in Fig. 15 for all 421 individual buildings. Compared to B3, B10 is allocated fewer response tasks as a result of the microclimate interaction, as shown in Fig. 15(a). The conventional allocation based on average response density is implemented in Case 5. It can be seen in Fig. 15(c) that this method will lead to over- or under-respond in some buildings. In the up-regulated stage at 14:00, 112 individual buildings have indoor temperatures below the lower comfort limit, resulting in building over-response. Even more, in the down-regulated stage at 20:00, nearly 40% of the individual buildings have indoor temperatures above the upper comfort limit. Then, we implement the proposed capacity allocation strategy in Case 6, and the results are depicted in Fig. 15(b) and Fig. 15(d). Compared to B3, the response density distributions of all 421 individual buildings in B10 are closer to each other, primarily due to the similar

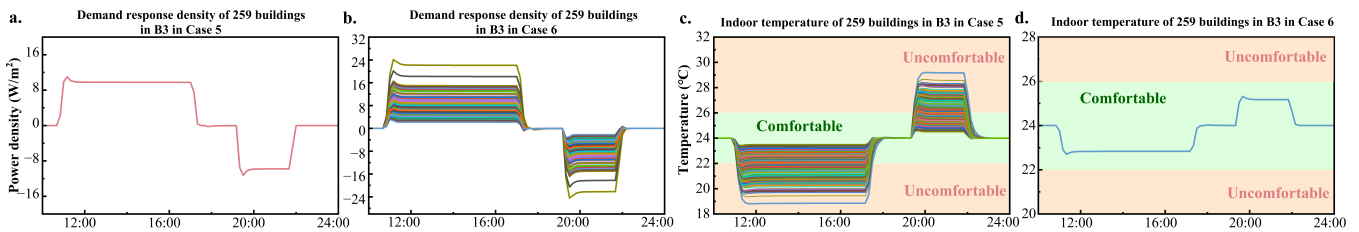


Fig. 14. Demand response results of B3 in Case 5 and Case 6.

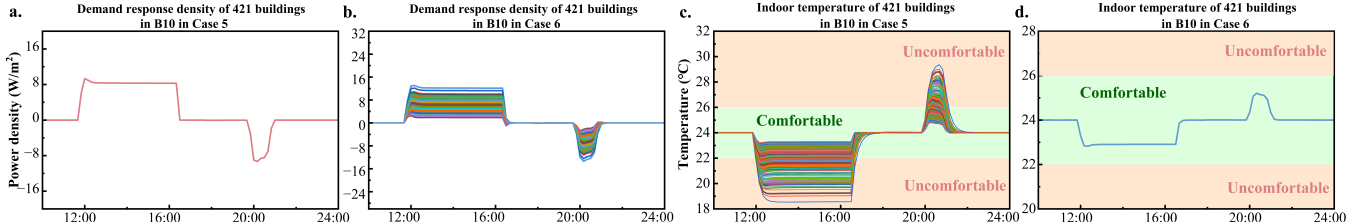


Fig. 15. Demand response results of B10 in Case 5 and Case 6.

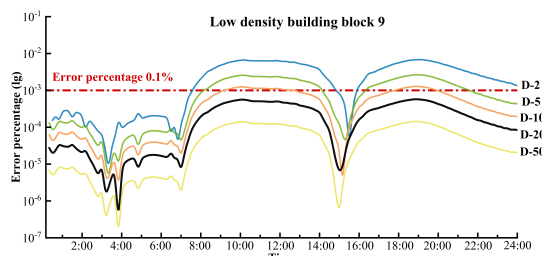


Fig. 16. Differential error percentage in building block 9.

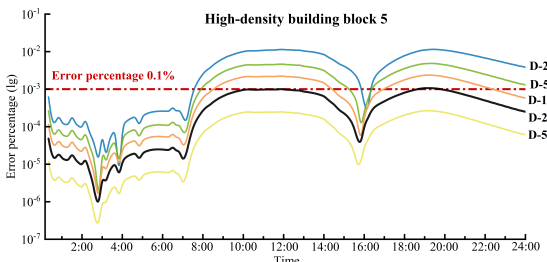


Fig. 17. Differential error percentage in building block 5.

structure of individual buildings in B10. Similar to B3, after the implementation of the SoC equalization, all the individual buildings in B10 achieve a consistent comfort curve, and demonstrating that strategy can effectively ensure response fairness.

D. Sensitivity Analysis for Differential Linearization

The differential linearization method is employed to solve the first-order differential equations of microclimate model in this paper. In the sensitivity analysis, we test the effect of different values of differential segments on the accuracy and efficiency of different building density blocks. First, we set the differential segments as 2, 5, 10, 20, and 50 in the low-density building block 9. The calculation error of urban

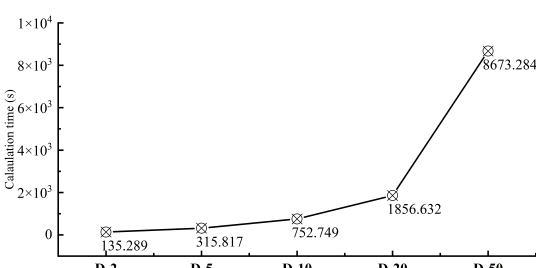


Fig. 18. The total calculation time in different differential segments.

canopy temperature distribution is depicted in Fig. 16. There are two main observations: a) Compared with the temperature distribution in Fig. 6 and error distribution, it can be seen that the level of error is related to the slope of change in temperature distribution. During periods of relatively stable temperatures, including the low-temperature period 0:00-7:00 and the high-temperature period 14:00-16:00, the error percentage is at a low level. On the contrary, during the periods of temperature change, including periods 8:00-14:00 and 17:00-22:00, the error percentage is at a high level. b) Compared with the different differential segment settings, it can be seen that when the value is up to 20, the error percentages of all dispatch periods are lower than 0.1%. Furthermore, the sensitivity analysis results in high-density building block 5 are depicted in Fig. 17. It can be seen that the error percentage curves of B9 and B5 have similar change trends. Besides, resulting from the higher slope of change in high-density building blocks, the entirety errors in different differential segments are higher than in low-density building blocks. Then, the total calculation time in different differential segments is depicted in Fig. 18. It can be seen that with the setting differential segment increasing, especially over 20, the calculation time will substantially rise. Therefore, based on the error percentage and calculation time analysis, the differential segment can be set as 20 to achieve better accuracy and efficiency.

V. CONCLUSION

This paper proposes a two-stage optimal response capacity allocation model considering the interaction between ACs and surrounding microclimate. This model employs: (i) an urban microclimate model to explicitly describe temperature distribution in urban canopy layer, urban surface layer, and building envelop layer; (ii) an ACs model to describe the power consumption and virtual energy storage state with surrounding microclimate. In the first stage, all LAGs participate in the grand coalition and the designed benefit-sharing scheme keeps cooperation solid. In the second stage, the SoC equalization is implemented to ensure the response fairness for individual buildings. The main conclusions are as follows:

- 1) There is a clear interaction between ACs and surrounding microclimate. In the high-density building block of Macau peninsula, the interaction involving ACs in-

creased 2.96°C in the maximum urban canopy temperature and a 2.81°C rise in the maximum building envelope temperature. Correspondingly, the increased energy consumption has surpassed 30%.

- 2) The two-stage optimal response capacity allocation leads to an overall increase in total benefits by 36.94%, demonstrating the efficiency of optimized cooperative strategies. The designed benefit-sharing scheme achieve reasonable redistribution based on the marginal contribution of each LAGs. The proposed approach ensures that the indoor temperatures of all individual buildings remain with the comfort zone.

When the penetration of air conditioners is significantly high in the future, the interaction among air conditioner operation, building cooling demand, and the microclimate surrounding buildings becomes more severe. The dynamic coefficiency of performance model of air conditioners will attract more attention on the effect of these interactions. Additionally, the energy cascade utilization will be a promise way to ease the interaction, combining the multi-energy conversion units and renewable energy generation.

REFERENCES

- [1] M. O. Qays, I. Ahmad, D. Habibi, A. Aziz, and T. Mahmoud, "System strength shortfall challenges for renewable energy-based power systems: A review," *Renewable and Sustainable Energy Reviews*, p. 113447, 2023.
- [2] H. Gao, T. Jin, C. Feng, C. Li, Q. Chen, and C. Kang, "Review of virtual power plant operations: Resource coordination and multidimensional interaction," *Applied Energy*, vol. 357, p. 122284, 2024.
- [3] L. Ma, H. Hui, and Y. Song, "Data valuation-aware coordinated optimization of power-communication coupled networks considering hybrid ancillary services," *IEEE Transactions on Smart Grid*, 2024.
- [4] IEA, "Space cooling," URL <https://www.iea.org/reports/space-cooling-2>, 2023.
- [5] H. Li, Z. Ren, A. Trivedi, D. Srinivasan, and P. Liu, "Optimal planning of dual-zero microgrid on an island toward net-zero carbon emission," *IEEE Transactions on Smart Grid*, vol. 15, no. 2, pp. 1243–1257, 2024.
- [6] M. Song, W. Sun, et al., "Robust distribution system load restoration with time-dependent cold load pickup," *IEEE Transactions on Power Systems*, vol. 36, no. 4, pp. 3204–3215, 2020.
- [7] T. Xu, T. Chen, C. Gao, and H. Hui, "Intelligent home energy management strategy with internal pricing mechanism based on multiagent artificial intelligence-of-things," *IEEE Systems Journal*, vol. 17, no. 4, pp. 6045–6056, 2023.
- [8] T. Qi, C. Ye, H. Hui, and Y. Zhao, "Fast frequency regulation utilizing non-aggregate thermostatically controlled loads based on edge intelligent terminals," *IEEE Transactions on Smart Grid*, vol. 15, no. 4, pp. 3571–3584, 2024.
- [9] L. Yang, H. Li, H. Zhang, Q. Wu, and X. Cao, "Stochastic-distributionally robust frequency-constrained optimal planning for an isolated microgrid," *IEEE Transactions on Sustainable Energy*, early access, 2024.
- [10] Z. Wang and H. Zhang, "Customized load profiles synthesis for electricity customers based on conditional diffusion models," *IEEE Trans. Smart Grid*, vol. 15, no. 4, pp. 4259–4270, 2024.
- [11] Z. Li, Y. Xu, P. Wang, and G. Xiao, "Restoration of a multi-energy distribution system with joint district network reconfiguration via distributed stochastic programming," *IEEE Transactions on Smart Grid*, vol. 15, no. 3, pp. 2667–2680, 2024.
- [12] R. E. Hedegaard, M. H. Kristensen, T. H. Pedersen, A. Brun, and S. Petersen, "Bottom-up modelling methodology for urban-scale analysis of residential space heating demand response," *Applied Energy*, vol. 242, pp. 181–204, 2019.
- [13] Z. Zhang, C. Wang, Q. Wu, and X. Dong, "Optimal dispatch for cross-regional integrated energy system with renewable energy uncertainties: A unified spatial-temporal cooperative framework," *Energy*, vol. 292, p. 130433, 2024.
- [14] M. Song, R. Deng, X. Yan, W. Sun, C. Gao, M. Yan, M. Ban, and S. Xia, "Two-stage decision-dependent demand response driven by tcls for distribution system resilience enhancement," *Applied Energy*, vol. 361, p. 122894, 2024.
- [15] X. Yin, C. Ye, Y. Ding, Y. Song, and L. Wang, "Combined heat and power dispatch against cold waves utilizing responsive internet data centers," *IEEE Transactions on Sustainable Energy*, vol. 15, no. 2, pp. 819–834, 2024.
- [16] H. Gao, T. Jin, K. Zheng, S.-J. Ahn, and C. Kang, "Dynamic construction and enhanced control of vpps considering trade matching in iot-based local energy system," *IEEE Internet of Things Journal*, vol. 11, no. 14, pp. 24523–24537, 2024.
- [17] P. Rajagopal, R. S. Priya, and R. Senthil, "A review of recent developments in the impact of environmental measures on urban heat island," *Sustainable Cities and Society*, vol. 88, p. 104279, 2023.
- [18] M. Martin, A. Afshari, P. R. Armstrong, and L. K. Norford, "Estimation of urban temperature and humidity using a lumped parameter model coupled with an energyplus model," *Energy and Buildings*, vol. 96, pp. 221–235, 2015.
- [19] A. Kumar, *Earth Observation in Urban Monitoring: Techniques and Challenges*. Elsevier Limited, 2024.
- [20] N. Antoniou, H. Montazeri, M. Neophytou, and B. Blocken, "Cfd simulation of urban microclimate: Validation using high-resolution field measurements," *Science of the total environment*, vol. 695, p. 133743, 2019.
- [21] L. Zhao, X. Lee, R. B. Smith, and K. Oleson, "Strong contributions of local background climate to urban heat islands," *Nature*, vol. 511, no. 7508, pp. 216–219, 2014.
- [22] Y. Sun, X. Zhang, G. Ren, F. W. Zwiers, and T. Hu, "Contribution of urbanization to warming in china," *Nature Climate Change*, vol. 6, no. 7, pp. 706–709, 2016.
- [23] P. Rajagopalan, K. C. Lim, and E. Jamei, "Urban heat island and wind flow characteristics of a tropical city," *Solar Energy*, vol. 107, pp. 159–170, 2014.
- [24] M. T. Craig, J. Wohland, L. P. Stoop, A. Kies, B. Pickering, H. C. Bloomfield, J. Browell, M. De Felice, C. J. Dent, A. Deroubaix, et al., "Overcoming the disconnect between energy system and climate modeling," *Joule*, vol. 6, no. 7, pp. 1405–1417, 2022.
- [25] K. Javanroodi, V. M. Nik, M. G. Giometto, and J.-L. Scartezzini, "Combining computational fluid dynamics and neural networks to characterize microclimate extremes: Learning the complex interactions between meso-climate and urban morphology," *Science of The Total Environment*, vol. 829, p. 154223, 2022.
- [26] Y. Liu, Q. Li, L. Yang, K. Mu, M. Zhang, and J. Liu, "Urban heat island effects of various urban morphologies under regional climate conditions," *Science of the total environment*, vol. 743, p. 140589, 2020.
- [27] V. Masson, "A physically-based scheme for the urban energy budget in atmospheric models," *Boundary-layer meteorology*, vol. 94, pp. 357–397, 2000.
- [28] B. Bueno, J. Hidalgo, G. Pigeon, L. Norford, and V. Masson, "Calculation of air temperatures above the urban canopy layer from measurements at a rural operational weather station," *Journal of Applied Meteorology and Climatology*, vol. 52, no. 2, pp. 472–483, 2013.
- [29] Y. Wen and Z. Lian, "Influence of air conditioners utilization on urban thermal environment," *Applied Thermal Engineering*, vol. 29, no. 4, pp. 670–675, 2009.
- [30] Y. Kikegawa, Y. Genchi, H. Kondo, and K. Hanaki, "Impacts of city-block-scale countermeasures against urban heat-island phenomena upon a building's energy-consumption for air-conditioning," *Applied Energy*, vol. 83, no. 6, pp. 649–668, 2006.
- [31] Y. Ohashi, Y. Genchi, H. Kondo, Y. Kikegawa, H. Yoshikado, and Y. Hirano, "Influence of air-conditioning waste heat on air temperature in tokyo during summer: Numerical experiments using an urban canopy model coupled with a building energy model," *Journal of Applied Meteorology and climatology*, vol. 46, no. 1, pp. 66–81, 2007.
- [32] B. Bueno, L. Norford, J. Hidalgo, and G. Pigeon, "The urban weather generator," *Journal of Building Performance Simulation*, vol. 6, no. 4, pp. 269–281, 2013.
- [33] N. Centre URL <http://data.cma.cn/>.
- [34] S. Xia, L. Cai, M. Tong, T. Wu, P. Li, and X. Gao, "Regulation flexibility assessment and optimal aggregation strategy of greenhouse loads in modern agricultural parks," *Protection and Control of Modern Power Systems*, 2024.
- [35] Z. Ji, X. Liu, and D. Tang, "Game-theoretic applications for decision-making behavior on the energy demand side: a systematic review," *Protection and Control of Modern Power Systems*, vol. 9, no. 2, pp. 1–20, 2024.

- [36] Y. Jiang, Z. Ren, and W. Li, "Committed carbon emission operation region for integrated energy systems: Concepts and analyses," *IEEE Transactions on Sustainable Energy*, vol. 15, no. 2, pp. 1194–1209, 2024.
- [37] R. J. Aumann and L. S. Shapley, *Values of non-atomic games*. Princeton University Press, 2015.
- [38] L. Yan, X. Chen, Y. Chen, and J. Wen, "A cooperative charging control strategy for electric vehicles based on multiagent deep reinforcement learning," *IEEE Transactions on Industrial Informatics*, vol. 18, no. 12, pp. 8765–8775, 2022.
- [39] I. of Geographic Sciences and C. Natural Resources Research, "Resource and environment science and data center," URL <https://www.resdc.cn/data.aspx?DATAID=270>.



Zhenwei Zhang (Graduate Student Member, IEEE) received the M.S. degrees in Electrical Engineering from Shandong University, Jinan, China, in 2022.

Now, he is pursuing the Ph.D. degree in Electrical and Computer Engineering at University of Macau, Macao SAR, China. His research focuses on the coupling between urban microclimate and urban energy system, demand-side resources management, optimal operation of integrated energy system.



Hongxun Hui (Member, IEEE) received the B.E. and Ph.D. degrees in electrical engineering from Zhejiang University, Hangzhou, China, in 2015 and 2020, respectively.

From 2018 to 2019, he was a visiting scholar with the Advanced Research Institute, Virginia Tech, and the CURENT Center, University of Tennessee. He is currently an Assistant Professor with the State Key Laboratory of Internet of Things for Smart City, University of Macau, Macao SAR, China. His research interests include optimization and control of power system, demand response, and Internet of Things technologies for smart energy.



Yonghua Song (Fellow, IEEE) received the B.E. degree from Chengdu University of Science and Technology, Chengdu, China, in 1984, and the Ph.D. degree from China Electric Power Research Institute, Beijing, China, in 1989, both in electrical engineering.

From 1989 to 1991, he was a Postdoctoral Fellow with Tsinghua University, Beijing, China. He then held various positions with Bristol University, Bristol, U.K.; Bath University, Bath, U.K.; John Moores University, Liverpool, U.K., from 1991 to 1996. In 1997, he was a Professor of Power Systems with Brunel University, where he has been a Pro-Vice Chancellor for Graduate Studies since 2004. In 2007, he took up a Pro-Vice Chancellorship and Professorship of Electrical Engineering with the University of Liverpool, Liverpool. In 2009, he was with Tsinghua University as a Professor of Electrical Engineering and an Assistant President and the Deputy Director with the Laboratory of Low-Carbon Energy. During 2012 to 2017, he was the Executive Vice President with Zhejiang University, as well as Founding Dean of the International Campus and Professor of Electrical Engineering and Higher Education of the University. Since 2018, he has been Rector of the University of Macau and the Director with the State Key Laboratory of Internet of Things for Smart City. His current research interests include smart grid, electricity economics, and operation and control of power systems.

Dr. Song was elected as the Vice-President of Chinese Society for Electrical Engineering (CSEE) and appointed as the Chairman of the International Affairs Committee of the CSEE in 2009. In 2004, he was elected as a Fellow of the Royal Academy of Engineering, U.K. In 2019, he was elected as a Foreign Member of the Academia Europaea. He was the recipient of D.Sc. by Brunel University in 2002, Honorary D.Eng. by the University of Bath in 2014, and Honorary D.Sc. by the University of Edinburgh in 2019.